

# Large-Area Antenna-Assisted SEIRA Substrates by Laser Interference Lithography

Shahin Bagheri, Harald Giessen, and Frank Neubrech\*

Laser interference lithography is utilized to fabricate large-area plasmonic antenna substrates for surface-enhanced infrared absorption (SEIRA). Changing the interference condition in each exposure process allows precise control over the geometrical parameters of the structures and thus tailoring of their optical response. Independent of the underlying wafer, the technique enables a homogeneous preparation of antennas over cm<sup>2</sup> areas with tunable and high-quality plasmonic resonances in the near- and mid-infrared spectral range. The broad applicability of such SEIRA substrates is demonstrated by enhancing the infrared vibrational signals of a monolayer octadecanethiol and by monitoring the ultraviolet degradation of a polymer via the decrease of its specific vibrational modes. Due to the large-area and fast fabrication process, laser interference lithography is ideally suited for the preparation of low-cost sensing platforms for a variety of different SEIRA applications in the chemical, analytical, and life sciences.

and low-cost fabrication is required. Ideally, one would like to have low-cost and cm<sup>2</sup> sized chips, which provide plasmonic resonance over the whole area and can be simply put into standard infrared spectrometers, serving as smart substrates for the detection and identification of biological or chemical substances. Randomly distributed metal island films<sup>[10,11]</sup> or metal stripe gratings<sup>[12]</sup> enable such large-area fabrication, but their plasmonic enhancement is orders of magnitudes smaller than the one of tailored nanoantennas. In contrast, metal antennas prepared by bottom-up approaches, such as nanosphere lithography,<sup>[13–15]</sup> offer higher enhancements but suffer from inhomogeneity on large scales. Recently, colloidal hole mask lithography<sup>[16,17]</sup> has been introduced as an

## 1. Introduction

Infrared (IR) spectroscopy is a standard tool in life science and medicine for the detection and chemical characterization of molecular species, since it allows for an unambiguous identification based on the specific molecular vibrations. Unfortunately, these molecular vibrations are excited inefficiently with infrared light. Thus, the detection of minute amounts of toxic or harmful<sup>[1,2]</sup> substances, which is essential for sensing applications, is hampered. One way to overcome this limitation is the use of specially designed metal structures, known as resonant plasmonic antennas. Such structures concentrate electromagnetic radiation in nanometer-sized volumes and therefore provide huge near-field enhancements (see Figure 1a and ref. [3]). Molecular vibrations of species located in these hot spots can be enhanced up to five orders in comparison to conventional infrared spectroscopy.<sup>[4–6]</sup>

Several studies following this approach of antenna-assisted surface-enhanced infrared absorption (SEIRA) utilize small-area samples fabricated by cost-intensive and time-consuming electron-beam lithography.<sup>[5,7–9]</sup> To transfer the high sensitivity enabled by antenna-assisted SEIRA to life science laboratories and to allow for a broad range of sensing applications a fast, large-area

approach to fabricate tailored nanostructures that provide high near-field enhancements. However, due to intrinsic limitations of the method, only randomly distributed antennas can be realized. Other methods, like nanoimprint techniques, have their own limitation such as a slow fabrication process of mask.<sup>[18–20]</sup> In contrast laser interference lithography enables a fast preparation of tailored polymer and metal structures arranged in well-defined geometries on large scales up to 4 inches,<sup>[21]</sup> with a high structure density.<sup>[22]</sup> These characteristics make laser interference lithography a powerful tool for the fabrication of plasmonic materials with a broad range of applications, for example, plasmonic color filtering<sup>[23]</sup> or biosensing.<sup>[24,25]</sup> Also, the fabrication of substrates for antenna-assisted SEIRA is enabled by this flexible approach as we will demonstrate in this paper.

In particular, we will highlight the potential of laser interference lithography as a powerful tool for the fast and low-cost preparation of homogeneous large-area substrates for antenna-assisted SEIRA. More specifically, we utilized laser interference lithography to prepare tailored metal structures featuring high-quality plasmon resonances in the near- and mid-infrared spectral range. These substrates provide excellent SEIRA activity as we demonstrate with two different molecular layers attached to the antennas. Furthermore, they enable sensitive in situ monitoring of the UV degradation of polymers via the signal contrast in their vibrational spectra.

## 2. Laser Interference Lithography

The interference of two coherent laser beams with wavelength  $\lambda$  causes a standing wave grating pattern which can be used

S. Bagheri, Prof. H. Giessen, Dr. F. Neubrech  
4th Physics Institute and Research Center SCoPE  
University of Stuttgart, Pfaffenwaldring 57  
70569 Stuttgart, Germany  
E-mail: f.neubrech@pi4.uni-stuttgart.de



DOI: 10.1002/adom.201400218

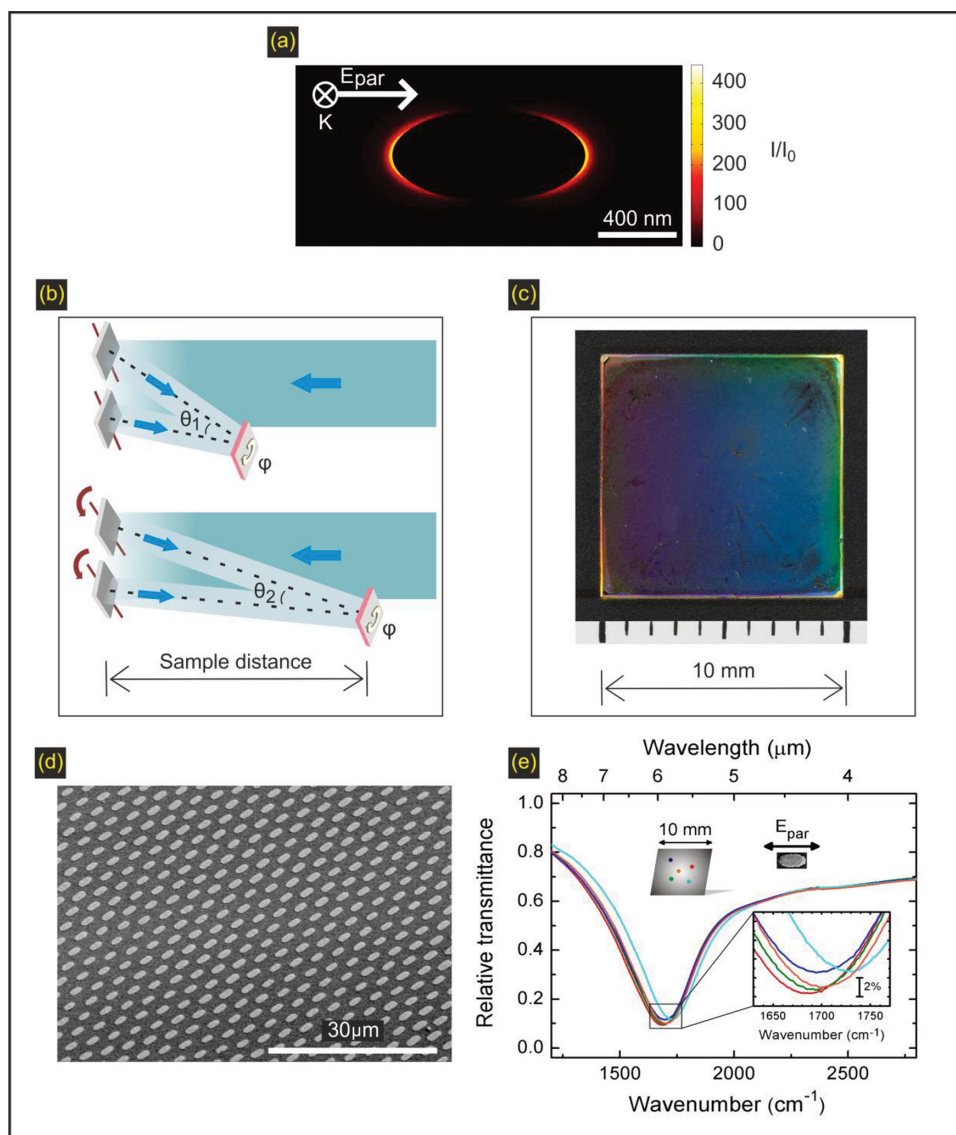


**Figure 1.** (a) Numerically calculated electromagnetic near-field intensity  $I/I_0$  (18 nm above the  $\text{CaF}_2$  substrate, parallel polarization) of an ellipsoidal antenna (length  $L = 1.0 \mu\text{m}$ , width  $W = 0.5 \mu\text{m}$ , and height  $H = 35 \text{ nm}$ ) resonant at  $3380 \text{ cm}^{-1}$ . The electromagnetic near-field intensity is concentrated in hot spots at the antenna tip ends. (b) Schematic view of our laser interference lithography set up: The expanded laser beam (blue-green) is directed by two mirrors to the gold and photoresist-covered wafer. This wafer is rotated by an angle  $\varphi$  (in this work  $53^\circ$ ) for a second exposure process in order to obtain 2D periodic structures. Antennas with various geometrical parameters (length, width and distance between antennas) are produced by changing the interference angle  $\theta$ . This is realized by moving the sample holder in direction of the expanded laser beam, thus changing the sample distance, and controlling the direction of the reflected light (sky blue) by tuning the mirrors. The photograph (c) and the scanning electron micrograph (d), tilted view) of gold antennas (length:  $2.1 \mu\text{m}$ , width:  $1 \mu\text{m}$ , height:  $35 \text{ nm}$ ) demonstrate the excellent homogeneity of our substrates on a large scale. The homogeneity is further confirmed by infrared transmittance measurement (parallel polarization,  $E_{\text{par}}$ ) recorded at different positions of the antenna substrate (e).

for the preparation of tailored structures in photoresists and optionally transferred to metals via etching processes. Tuning the periodicity ( $p$ )

$$p = \lambda / (2 \times \sin(\theta / 2)) \quad (1)$$

of this grating pattern by changing the angle  $\theta$  between the two incident beams and adding a second exposure step enables the fabrication of geometrically tunable structures.<sup>[26]</sup> Here, we utilize such a two-exposure process to fabricate large-area and

defect-free plasmonic antenna arrays for antenna-assisted surface-enhanced infrared absorption.

A schematic drawing of our laser interference lithography setup is shown in Figure 1b. Two parts of an expanded HeCd laser beam at  $325 \text{ nm}$  wavelength are selected with movable mirrors and directed towards the sample. The first UV exposure process generates a grating pattern in a photoresist which is spun onto a metal film (in our case gold) on the sample. Subsequently a second grating pattern with different orientation is achieved after rotating the sample (angle  $\varphi$  which is  $53^\circ$  for this

work) and exposing the photoresist a second time. Tuning the exposure dose for each step enables us to employ the double-exposed areas as a mask for antennas, which can be used for a flexible preparation independent of the underlying wafer. The pattern is then transferred via directional argon ion beam etching into the metal film, resulting in large-area regular arrays of metallic antennas with tunable lengths and widths as well as periodicities. For more details please see Experimental Section.

As a result of the sample fabrication process, we obtain highly homogenous antenna substrates on large scales ( $10 \times 10 \text{ mm}^2$ ) as shown in the photograph (Figure 1c) and the scanning electron microscopy (SEM) image (Figure 1d). This finding is also supported by the infrared optical properties of our antenna substrates. Typical infrared transmittance spectra recorded at various positions of such a sample feature plasmonic antenna resonances with frequencies and extinction varying by less than 3 % (Figure 1e). This excellent homogeneity of our large-area antenna substrates enables routine measurements with cm-sized apertures in simple standard FTIR spectrometers as they are present in many life sciences, chemistry and pharmacy laboratories. For a demonstration we acquired the transmittance of an antenna substrate ( $L = 1.8 \text{ }\mu\text{m}$  and  $W = 0.8 \text{ }\mu\text{m}$ ) with a simple FTIR spectrometer (Bruker Alpha) and a high-end FTIR spectrometer combined with an IR microscope. As expected we found a good agreement (see Figure S1 in the Supporting Information).

It is a well-known fact that the resonance frequencies of metal particles are tunable by their geometrical dimensions.<sup>[4,27]</sup> In our experiments, these geometrical parameters, such as length (L), width (W), and distance between the antennas cannot be chosen completely independently and are linked via simple geometrical relations:

$$L = \Delta a(p) / \sin(\varphi/2) \quad (2)$$

$$W = \Delta a(p) / \cos(\varphi/2) \quad (3)$$

As mentioned before, the rotation angle is given by  $\varphi$  and the photoresist linewidth by  $\Delta a$ , depending on the periodicity  $p$ . According to these equations and Equation (1) we can, for example, adjust the periodicity by changing the interference angle  $\theta$  for a constant ratio of length and width. Additionally we are able to control the antenna geometry by using different exposure doses or different development times of the photoresist. Larger antennas are fabricated with a higher exposure dose or shorter development time, whereas smaller antennas are produced with lower exposure dose or longer development time. These parameter variations enable us to prepare micro- and sub-micrometer-sized structures in different geometries on a large scale with plasmon resonances in the near- and mid-infrared spectral range.

### 3. Plasmonic Response of Large-Area Antenna Substrates

To demonstrate the capability of our method to precisely control the geometrical parameters of metal antennas and consequently the tuning of their plasmon resonances, SEM images and typical relative transmittance spectra of five different antenna substrates are shown in Figure 2.

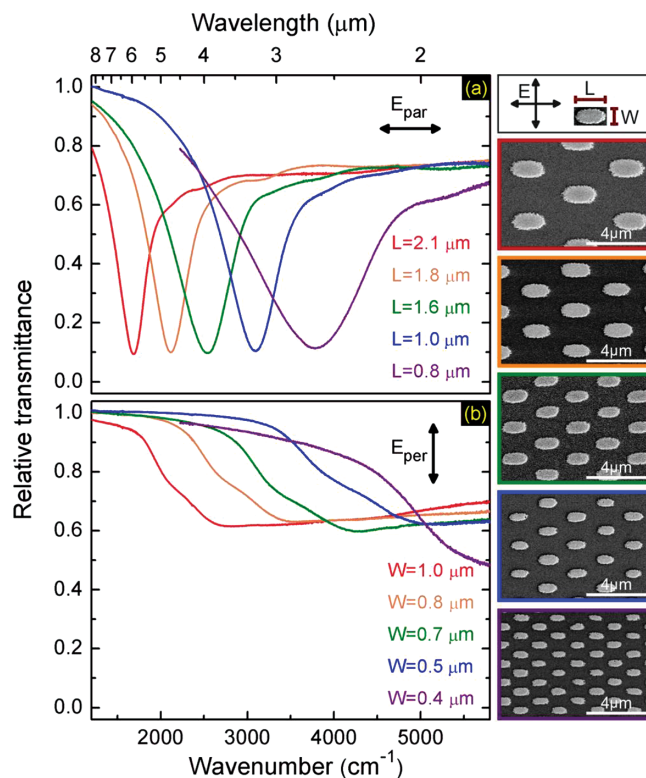


**Figure 2.** SEM images and typical relative transmittance spectra of gold antenna arrays prepared by laser interference lithography featuring tunable IR plasmonic resonances for (a) parallel ( $E_{\text{par}}$ ) and (b) perpendicular ( $E_{\text{per}}$ ) polarization (see upper right panel). The antennas are placed on  $\text{CaF}_2$  (red, orange, green and blue) and glass wafers (purple). Lengths (L) and corresponding standard deviations are  $(2.1 \pm 0.04) \text{ }\mu\text{m}$ ,  $(1.8 \pm 0.02) \text{ }\mu\text{m}$ ,  $(1.6 \pm 0.04) \text{ }\mu\text{m}$ ,  $(1 \pm 0.04) \text{ }\mu\text{m}$ ,  $(0.8 \pm 0.02) \text{ }\mu\text{m}$ . Widths (W) of the antennas and corresponding standard deviations are  $(1 \pm 0.02) \text{ }\mu\text{m}$ ,  $(0.8 \pm 0.02) \text{ }\mu\text{m}$ ,  $(0.7 \pm 0.02) \text{ }\mu\text{m}$ ,  $(0.5 \pm 0.02) \text{ }\mu\text{m}$ ,  $(0.4 \pm 0.03) \text{ }\mu\text{m}$ . The height of antennas is 35 nm and their distances are different for each sample due to the fabrication process. The error in height results from the evaporation process whereas the deviations in length and width of the antennas are mainly caused by the photoresist. Typical angles  $\theta$  range from 4 to 16 degrees.

The lengths (L) and widths (W) of the antennas vary from 2.1 to 0.8  $\mu\text{m}$  and 1 to 0.4  $\mu\text{m}$ , respectively, resulting in tunable plasmon resonances in the near- and mid-infrared spectral range (2.5 to 6.2  $\mu\text{m}$ ) with modulation depths up to 90 % for parallel polarization independent of the underlying wafer (Figure 2a). On the contrary, plasmon resonances measured with perpendicularly polarized light (Figure 2b) are less intense and much broader, mainly resulting from smaller dipole moments.<sup>[28]</sup> Besides the fundamental resonance a variety of resonant modes are observed for both polarizations. Some of them have their origin in higher order excitations;<sup>[29]</sup> others are due to collective modes.<sup>[30]</sup> Such Rayleigh anomalies stem from the coupling of densely packed and periodically arranged metal structures<sup>[31]</sup> with distances in the range of the resonant wavelength as present. This coupling behavior combined with the low aspect ratio of our antennas causes a non-linear dependency of the infrared resonant wavelength on the antenna length in contrast to single nanoantennas with high aspect ratio.<sup>[32]</sup>

As mentioned above our laser interference lithography setup has been designed especially for a precise control of the antenna parameters in order to achieve large tunability of plasmon resonances in the near- and mid- infrared independent of the underlying wafer (Figure 2). For example, silicon as underlying wafer is also feasible, however it will reduce the SEIRA enhancement due to its higher refractive index.<sup>[14]</sup> One can easily extend the spectral range to lower or higher energies by changing the interference conditions. For instance, smaller interference angles  $\theta$  will enable the fabrication of larger antennas with plasmon resonances located at larger wavelengths. In contrast to that, using the maximum interference angle ( $\theta = 90^\circ$ ) will allow for a preparation of nanometer-sized antennas ( $L = 100$  nm and  $W = 50$  nm), with particle plasmon resonances in visible spectral range.

#### 4. Antenna-Assisted Surface-Enhanced Infrared Absorption

The large tunability range, high modulation depths, and a homogeneous sample preparation make our antenna substrates ideally suited for sensing applications based on surface-enhanced infrared absorption. The only precondition for SEIRA, however, is a good overlap between the plasmonic excitation of the antennas and the molecular vibration. Consequently, tailored antenna arrays are required which can be easily prepared with laser interference lithography as shown in Figure 2a. In order to demonstrate the SEIRA activity of our large-area substrates, we covered two different samples with an octadecanethiol (ODT) monolayer and a 30 nm thick photoresist film, respectively.

ODT<sup>[33]</sup> has been introduced before as a self-assembled monolayer on gold surfaces in SEIRA experiments.<sup>[4]</sup> Since the adsorption requires a clean gold surface, we treated our substrate with oxygen plasma before we immersed it into an ODT solution to attach ODT molecules to the gold antennas (see Experimental Section). A typical relative transmittance spectrum of antennas covered with ODT is shown in Figure 3a. The plasmonic resonance frequency is tailored to the symmetric and asymmetric  $\text{CH}_2$  vibrations of the ODT molecules for light polarized parallel to the long wire axis. Additionally, for perpendicular polarization, enhanced ODT vibrational bands are found.

To quantitatively evaluate the vibrational signal enhancement, we performed a baseline correction introduced by Eilers.<sup>[34]</sup> This algorithm allows us to remove any spectral features caused by the antenna and thus provides the undisturbed line shape of the enhanced signal (see Figure 3c). As known from other studies<sup>[4,6,35]</sup> and clearly seen in our measurements, the enhanced vibrational signals exhibit a characteristic Fano-type behavior resulting from the coupling of the plasmonic and vibrational excitation. The detailed shape of the vibrational band, in our case an asymmetric structure, is given by the phase between the plasmonic and the vibrational excitation and changes with the spectral position of the resonance relative to the vibrational band.<sup>[36,37]</sup> It is worth mentioning that also for perpendicular polarization a significant vibrational signal, defined as the difference between minimum and

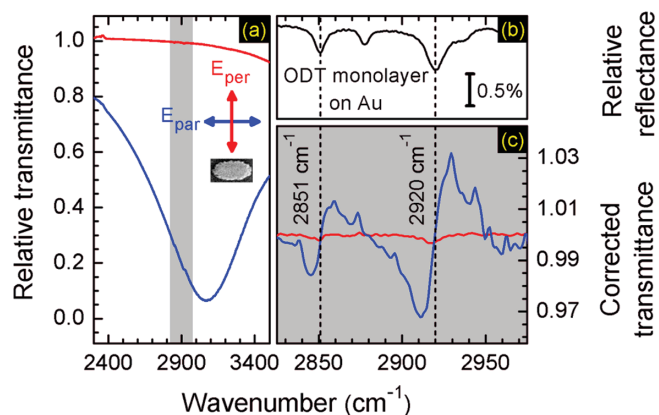


**Figure 3.** (a) Typical relative IR transmittance spectrum of antennas covered with a monolayer of ODT measured with parallel,  $E_{\text{par}}$  (blue), and perpendicular,  $E_{\text{per}}$  (red), polarized light. For parallel polarization the plasmonic resonance is tuned to the ODT vibrational bands to obtain highest enhancement. (b) IR reflection absorption measurements of one monolayer ODT adsorbed on a flat gold wafer. (c) Zoom to the baseline corrected transmittance showing the ODT vibration modes ( $2851$   $\text{cm}^{-1}$  and  $2920$   $\text{cm}^{-1}$ , dashed lines) for parallel and perpendicular polarizations. Due to the better resonance match, a higher enhancement is observed for the parallel polarization.

maximum (0.3% for asymmetric and 0.2% for symmetric  $\text{CH}_2$  stretching modes of ODT), is observed. However, it is much smaller due to the worse resonance match in comparison to parallel polarization, where we extract values of 6.4% and 2.8%, respectively. Furthermore even for a similar match, we have to expect less signal enhancement due to the lower dipole strength of the antenna modes excited along the antenna short axis.<sup>[28]</sup>

Infrared reflection absorption spectroscopy (IRRAS) of an ODT monolayer on a gold layer (Figure 3b) is used to estimate an enhancement factor. Based on Fresnel's equations for a three-layer system, the measured reflection change is converted to an IR transmission change ( $I_{\text{calc}} = 0.0087\%$  for the asymmetric  $\text{CH}_2$  and  $0.0035\%$  for the symmetric  $\text{CH}_2$  stretching vibration)<sup>[4]</sup> and compared to the enhanced transmission signal ( $I_{\text{SEIRA}} = 6.4\%$  for the asymmetric  $\text{CH}_2$  and  $2.8\%$  for the symmetric  $\text{CH}_2$  mode) obtained from SEIRA studies. Furthermore, the relative fractions of illuminated spot areas in IRRAS and SEIRA geometry need to be considered. Whereas in IRRAS the IR signal stems from the whole illuminated layer, in SEIRA only a small fraction of molecules actively contribute to the enhanced vibrational signal. These molecules are located in the highly confined near-field around the tip ends (see Figure 1a). For the estimation of an enhancement factor we therefore took the two end faces of the antenna as SEIRA active areas, i.e.,  $2 \times 500 \times 35$   $\text{nm}^2$ . This approximation was also suggested by D'Andrea et al.<sup>[28]</sup> Considering these effects, enhancement factors up to 72 000 are estimated for antennas resonantly tuned to the ODT vibrations. In contrast to that, enhancement factors up to 1500 are obtained if the entire antenna surface is considered to be SEIRA active. These factors are one order of magnitude lower than values reported for nanometer-sized antennas.<sup>[4,5]</sup> We attribute these differences to the relatively low aspect ratio of our antennas resulting in less confined electromagnetic near-fields. Furthermore, strong interaction between the structures

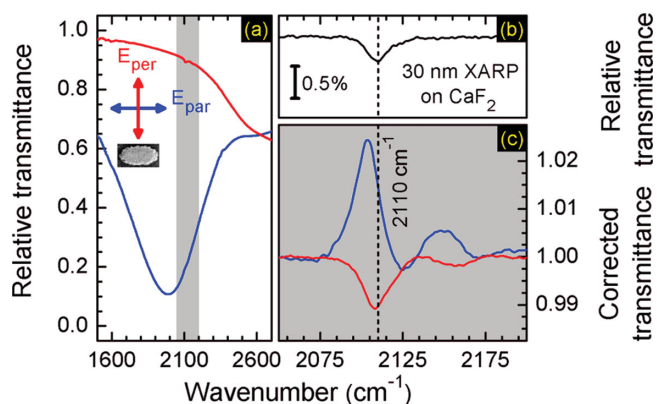


**Figure 4.** Antenna-assisted SEIRA of the spin-coated polymer XARP using large-area plasmonic substrates. (a) Typical relative IR transmittance spectrum of antennas covered with 30 nm of XARP for parallel,  $E_{\text{par}}$  (blue), and perpendicular,  $E_{\text{per}}$  (red), polarization. To achieve the highest enhancement the plasmonic resonance is tuned to the polymer vibration mode. (b) Relative IR transmittance spectra of 30 nm XARP spin-coated on a  $\text{CaF}_2$  wafer. (c) Baseline corrected transmittance (zoom in) of the polymer vibration mode ( $2110\text{ cm}^{-1}$ ) for parallel and perpendicular polarizations. Please note that we only consider the most prominent vibrational band at  $2110\text{ cm}^{-1}$  and neglect the less intense one at  $2134\text{ cm}^{-1}$ . Different near-field enhancements cause different signal enhancements for parallel and perpendicular polarization.

may lead to a suppression of the enhanced vibrational signals as discussed in ref. [38].

Our antenna substrates fabricated by laser interference lithography can not only be used for the detection of minute amounts of analytes but also for in situ monitoring of dynamic processes such as the UV degradation of polymers as we will demonstrate in the following. Therefore, we spin-coated our sample with a positive photoresist (XARP 3100/10) and monitored its UV degradation via the decrease of a selected vibrational band ( $2110\text{ cm}^{-1}$ ) when illuminating the polymer-covered sample with UV light ( $\lambda = 320\text{--}390\text{ nm}$ ).

In order to achieve the maximum signal enhancement we prepared antennas with spectrally tailored resonances close to the XARP vibration, covered them with a 30 nm thick layer of XARP and performed infrared transmittance measurements (Figure 4a). Please note that due to the spin-coating process no uniform XARP coverage of the antennas was achieved.

As expected we observe an increased vibration signature, which is a superposition of two vibrational signals originating from different sample areas. One part originates from the coupling with the antennas and features the characteristic asymmetric Fano-type line shape, while the other fraction stems from molecules located outside of the enhanced plasmonic near-fields, i.e., the area between the antennas. Since we are only interested in the enhanced vibrational signal we calculate the ratio of the spectrum measured with parallel (perpendicular) polarized light and the reference spectrum of XARP deposited on an unstructured calciumdifluoride ( $\text{CaF}_2$ ) wafer to obtain purely the antenna-enhanced XARP vibrational signal (Figure 4b). For further analysis the spectrum is baseline corrected and a signal strength of 2.7% for parallel polarization is extracted (Figure 4c). This value corresponds to an enhancement factor of about 900 if only the hot spots are taken into

account and 20 if the entire antenna surface is considered. Please note that we only focus on the most intense vibration at  $2110\text{ cm}^{-1}$  and do not consider the less intense vibration at  $2134\text{ cm}^{-1}$ , which shows a very similar behavior. In contrast to our ODT studies, we observed lower enhancement factors originating from the different deposited layer thicknesses of 30 nm for XARP and 2.8 nm for ODT.<sup>[33]</sup> The result is in qualitative agreement with recent studies, where the antenna-enhanced signal evolution with molecular layer thickness was investigated.<sup>[39]</sup> Due to the rapidly decaying near-fields of resonantly excited antennas, molecules located in the direct vicinity of the antennas are strongly enhanced, while vibrations of molecules located apart do not contribute significantly to the integrated signal, resulting in lower enhancements for thicker molecular layers.

The UV induced degradation of the above mentioned XARP polymer layer deposited on a structured and unstructured wafer is in situ monitored. As previously described, a normalization and subsequent baseline correction provides the antenna-enhanced vibrations for parallel (Figure 5a) and perpendicular (not shown) polarization.

The vibrational signals decrease with UV illumination time due to the decomposition of the polymer. To point out the degradation process in more detail, we plotted the signal (difference between minimum and maximum) in dependence of the illumination time (Figure 5b). Obviously, the vibrational signal strengths in both parallel and perpendicular polarizations are enhanced in comparison to reference measurements of the polymer layer spin-coated on an unstructured  $\text{CaF}_2$  wafer with the same thickness (black curve). For example, after 65 s of UV illumination, the unenhanced vibrational signal of the polymer is below the noise level and not detectable with conventional

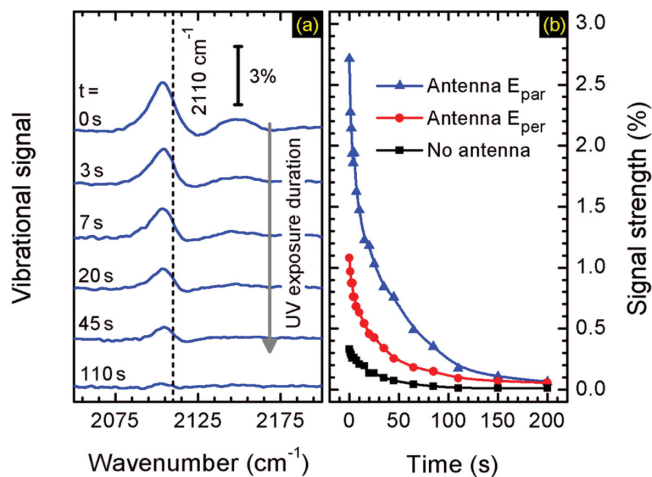


**Figure 5.** UV degradation of the photoresist XARP is monitored via the decrease of the selected vibrational mode at  $2110\text{ cm}^{-1}$ . (a) Baseline corrected IR spectra (parallel polarization,  $E_{\text{par}}$ ) show a decrease of the enhanced vibrational signal for different UV exposure times. The dashed line indicates the vibrational mode. (b) Signal strength (difference between minimum and maximum) of the antenna-enhanced vibrational mode as extracted from (a). As references the time traces are also shown for perpendicular polarization ( $E_{\text{per}}$ , red) and a wafer without any antennas (black). The errors of the vibrational signals are smaller than the symbol size.

infrared spectroscopy. In contrast to that, the enhanced signals are still visible. The slope of the curve, however, is not affected by the antennas, indicating that the confined electromagnetic near-fields do not influence the degradation behavior. Thus SEIRA can be used as reliable tool to monitor chemical processes with higher sensitivity without influencing the process itself.

## 5. Conclusion

We employed laser interference lithography to fabricate large plasmonic antenna arrays with an excellent homogeneity, featuring high quality plasmons in the near- and mid-infrared spectral range. Depending on the process parameters, the resonances are easily tunable and thus ideally suited for antenna-assisted surface-enhanced infrared absorption as we demonstrated for two molecular substances, namely octadecanethiol and the polymer XARP. The measured differences in signal enhancement (72 000 for octadecanethiol and 900 for the polymer) are related to the rapidly decaying near-fields, since the ODT molecules are directly adsorbed on the antennas whereas the polymer film extends over a range of 30 nm. In comparison to conventional infrared spectroscopy, however, the signal enhancement still provides significant improvement. For example, it was possible to in situ monitor the UV induced degradation of the XARP polymer with an increased sensitivity via vibrational signal decay without modifying the degradation process itself. These results demonstrate the capability of laser interference lithography to homogeneously fabricate plasmonic antennas on large areas with high quality resonances that can be specifically tailored for various antenna-assisted SEIRA applications.

## 6. Experimental Section

Prior to the laser interference lithography exposure, we cleaned the CaF<sub>2</sub> and glass wafers with acetone and iso-propanol for 10 minutes in an ultrasonic bath and subsequently dried them with nitrogen. After that we evaporated a 2 nm thick chromium layer (adhesion layer) followed by 35 nm thick gold layer (Pfeiffer Vacuum Model PLS-500, 10<sup>-7</sup> mbar) onto the wafer and spin-coated a 90 nm thick photoresist film (ma-N 405)<sup>[40]</sup> on top of the gold layer. For the subsequent UV exposure we used a HeCd laser (Kimmon Electric Co,  $\lambda = 325$  nm, 14 mW) as a light source and achieved an expanded Gaussian laser beam using a UV objective lens (Carl Zeiss, 10-fold magnification, NA = 0.2) and a 5  $\mu$ m pinhole. The samples were placed between 185 and 215 cm behind the pinhole. Typical UV exposure doses were between 0.8 and 2 mJ/cm<sup>2</sup> with typical exposure times between 25 and 45 s. After the exposure we immersed the samples in a developer (AZ826, development time between 25 and 40 s), distilled water for 60 s and dried them using nitrogen. Then the areas covered with the developed photoresist were transferred into the gold layer via an argon ion beam etching process (Technics Plasma Model R.I.B.-Etch 160, etching time 90 seconds) resulting in the gold structures of desired shape and size. Finally, the remaining photoresist was removed using acetone and iso-propanol.

Before the adsorption of octadecanethiol (ODT, Sigma Aldrich, 95%) we cleaned our antenna substrates using oxygen plasma (Diener electronic Plasma-Surface-Technology, 25 min, 1.3 mbar, 160 W) in order to remove any residues from the fabrication process. Subsequently the samples were immersed into a 1 mM ODT solution in pure ethanol for at least 48 hours. During that time a monolayer of ODT covalently

bound to the gold surface. Afterwards we rinsed the samples by ethanol several times to remove unbound ODT molecules and any other contaminations.

Infrared spectroscopy was performed using a Bruker Hyperion microscope (15-fold magnification, NA = 0.4) coupled to a Bruker Vertex 80 spectrometer, allowing for laterally resolved measurements on the micrometer-scale. Typical infrared spectra were recorded in parallel and perpendicular polarization with at least 25 scans and a resolution of 2 cm<sup>-1</sup>.

For the XARP (All Resist) degradation experiments we used a UV source (DYMAX Blue Wave 50,  $\lambda = 320$ – $390$  nm) with the fiber end placed approximately 3 cm away from the sample.

The near-field intensity distribution was calculated by numerically solving Maxwell's equations under normal incidence of infrared radiation polarized parallel to the long antenna axis using the commercial finite-difference time-domain (FDTD) software Lumerical FDTD-Solutions v8.5.3. Based on the fabricated structures the gold antenna was modeled as a vertical extrusion (height 35 nm) of an oval with length  $L = 1$   $\mu$ m, width  $W = 0.5$   $\mu$ m placed on a CaF<sub>2</sub> substrate. The substrate was described by a dispersionless refractive index of  $n = 1.41$  and the optical data of gold was taken from Palik.<sup>[41]</sup> The antenna was situated at least one wavelength size away from the perfect matched layers (PMLs) that describe the boundary conditions of the simulation volume. In order to reduce computational resources the total field scattered field (TFSF) approach and subgridding techniques were chosen. Typical mesh sizes of 2 nm were used in the vicinity of the antenna and mesh sizes smaller than 100 nm elsewhere. A plane wave from a broadband source (2000 cm<sup>-1</sup> to 5000 cm<sup>-1</sup>) excited the structure. The electromagnetic field intensities were recorded with a 2D field profile monitor placed parallel to the substrate at half height of the structure at the resonance frequency ( $\omega_{\text{res}} = 3380$  cm<sup>-1</sup>). Convergence testing was performed by iteratively reducing mesh sizes and increasing the number of PMLs, simulations times, and the simulation volume.

## Acknowledgements

The authors gratefully acknowledge financial support by ERC Advanced Grant COMPLEXPLAS as well as DFG, BMBF, GIF, Zeiss foundation, MWK Baden-Württemberg and the Baden-Württemberg Stiftung (PROTEINSENS, Spitzenforschung II).

Received: May 9, 2014

Revised: July 5, 2014

Published online: July 31, 2014

- [1] Y. Wang, K. Lee, J. Irudayaraj, *J. Phys. Chem. C* **2010**, *114*, 16122.
- [2] R. A. Halvorson, P. J. Vikesland, *Environ. Sci. Technol.* **2010**, *44*, 7749.
- [3] P. Mühlischlegel, H.-J. Eisler, O. J. F. Martin, B. Hecht, D. W. Pohl, *Science* **2005**, *308*, 1607.
- [4] F. Neubrech, A. Pucci, T. W. Cornelius, S. Karim, A. García-Etxarri, J. Aizpurua, *Phys. Rev. Lett.* **2008**, *101*, 157403.
- [5] R. Adato, H. Altug, *Nat. Commun.* **2013**, *4*, 2154.
- [6] R. Adato, A. A. Yanik, J. J. Amsden, D. L. Kaplan, F. G. Omenetto, M. K. Hongo, S. Erramilli, H. Altug, *Proc. Natl. Acad. Sci. USA* **2009**, *106*, 19227.
- [7] I. M. Pryce, Y. A. Kelaita, K. Aydin, H. A. Atwater, *ACS Nano* **2011**, *5*, 8167.
- [8] E. Cubukcu, S. Zhang, Y.-S. Park, G. Bartal, X. Zhang, *Appl. Phys. Lett.* **2009**, *95*, 043113.
- [9] H. Aouani, M. Rahmani, H. Šípová, V. Torres, K. Hegnerová, M. Beruete, J. Homola, M. Hong, M. Navarro-Cía, S. A. Maier, *J. Phys. Chem. C* **2013**, *117*, 18620.

- [10] C. V. Hoang, M. Oyama, O. Saito, M. Aono, T. Nagao, *Sci. Rep.* **2013**, *3*, 1175.
- [11] D. A. Perry, R. L. Borchers, J. W. Golden, A. R. Owen, A. S. Price, W. A. Henry, F. Watanabe, A. S. Biris, *J. Phys. Chem. Lett.* **2013**, *4*, 3945.
- [12] T. Wang, V. H. Nguyen, A. Buchenauer, U. Schnakenberg, T. Taubner, *Opt. Express* **2013**, *21*, 9005.
- [13] F. Le, D. W. Brandl, Y. A. Urzhumov, H. Wang, J. Kundu, N. J. Halas, J. Aizpurua, P. Nordlander, *ACS Nano* **2008**, *2*, 707.
- [14] J. M. Hoffmann, X. Yin, J. Richter, A. Hartung, T. W. W. Maß, T. Taubner, *J. Phys. Chem. C* **2013**, *117*, 11311.
- [15] Y.-C. Chang, S.-C. Lu, H.-C. Chung, S.-M. Wang, T.-D. Tsai, T.-F. Guo, *Sci. Rep.* **2013**, *3*, 3339.
- [16] S. Cataldo, J. Zhao, F. Neubrech, B. Frank, C. Zhang, P. V. Braun, H. Giessen, *ACS Nano* **2012**, *6*, 979.
- [17] B. Frank, X. Yin, M. Schäferling, J. Zhao, S. M. Hein, P. V. Braun, H. Giessen, *ACS Nano* **2013**, *7*, 6321.
- [18] S. Aksu, A. E. Cetin, R. Adato, H. Altug, *Adv. Opt. Mater.* **2013**, *1*, 798.
- [19] S. Aksu, A. A. Yanik, R. Adato, A. Artar, M. Huang, H. Altug, *Nano Lett.* **2010**, *10*, 2511.
- [20] V. Auzelyte, B. Gallinet, V. Flauraud, C. Santschi, S. Dutta-Gupta, O. J. F. Martin, J. Brugger, *Adv. Opt. Mater.* **2013**, *1*, 50.
- [21] W. Mao, I. Wathuthanthri, C.-H. Choi, *Opt. Lett.* **2011**, *36*, 3176.
- [22] R. Ji, W. Lee, R. Scholz, U. Gösele, K. Nielsch, *Adv. Mater.* **2006**, *18*, 2593.
- [23] Y. S. Do, J. H. Park, B. Y. Hwang, S.-M. Lee, B.-K. Ju, K. C. Choi, *Adv. Opt. Mater.* **2013**, *1*, 133.
- [24] Y. Shen, J. Zhou, T. Liu, Y. Tao, R. Jiang, M. Liu, G. Xiao, J. Zhu, Z.-K. Zhou, X. Wang, C. Jin, J. Wang, *Nat. Commun.* **2013**, *4*, 2381.
- [25] A. A. Yanik, A. E. Cetin, M. Huang, A. Artar, S. H. Mousavi, A. Khanikaev, J. H. Connor, G. Shvets, H. Altug, *Proc. Natl. Acad. Sci. USA* **2011**, *108*, 11784.
- [26] D. Xia, Z. Ku, S. C. Lee, S. R. J. Brueck, *Adv. Mater.* **2011**, *23*, 147.
- [27] H. Matsui, W. Badalawa, A. Ikehata, H. Tabata, *Adv. Opt. Mater.* **2013**, *1*, 397.
- [28] C. D'Andrea, J. Bochterle, A. Toma, C. Huck, F. Neubrech, E. Messina, B. Fazio, O. M. Maragò, E. Di Fabrizio, M. L. de La Chapelle, P. G. Gucciardi, A. Pucci, *ACS Nano* **2013**, *7*, 3522.
- [29] N. Verellen, F. López-Tejiera, R. Paniagua-Domínguez, D. Vercruyse, D. Denkova, L. Lagae, P. V. Dorpe, V. V. Moshchalkov, J. A. Sánchez-Gil, *Nano Lett.* **2014**, *14*, 2322.
- [30] A. O. Pinchuk, *J. Phys. Chem. A* **2009**, *113*, 4430.
- [31] A. Aizpurua, G. W. Bryant, L. J. Richter, F. J. García de Abajo, B. K. Kelley, T. Mallouk, *Phys. Rev. B* **2005**, *71*, 235420.
- [32] L. Novotny, *Phys. Rev. Lett.* **2007**, *98*, 266802.
- [33] F. Schreiber, *Prog. Surf. Sci.* **2000**, *65*, 151.
- [34] P. H. C. Eilers, *Anal. Chem.* **2003**, *75*, 3631.
- [35] M. Abb, Y. Wang, N. Papisimakis, C. H. de Groot, O. L. Muskens, *Nano Lett.* **2014**, *14*, 346.
- [36] V. Giannini, Y. Francescato, H. Amrania, C. C. Phillips, S. A. Maier, *Nano Lett.* **2011**, *11*, 2835.
- [37] E. J. Osley, C. G. Biris, P. G. Thompson, R. R. F. Jahromi, P. A. Warburton, N. C. Panoiu, *Phys. Rev. Lett.* **2013**, *110*, 087402.
- [38] D. Weber, P. Albella, P. Alonso-González, F. Neubrech, H. Gui, T. Nagao, R. Hillenbrand, J. Aizpurua, A. Pucci, *Opt. Express* **2011**, *19*, 15047.
- [39] F. Neubrech, S. Beck, T. Glaser, M. Hentschel, H. Giessen, A. Pucci, *ACS Nano* **2014**, *8*, 6250.
- [40] H. C. Guo, D. Nau, A. Radke, X. P. Zhang, J. Stodolka, X. L. Yang, S. G. Tikhodeev, N. A. Gippius, H. Giessen, *Appl. Phys. B* **2005**, *81*, 271.
- [41] E. D. Palik, *Handbook of Optical Constants of Solids*, Academic Press, NY, USA **1985**.